processes

MDPI

Article

Self-Supported Sheets-on-Wire CuO@Ni(OH)$_2$/Zn(OH)$_2$ Nanoarrays for High-Performance Flexible Quasi-Solid-State Supercapacitor

Jianyang Jiang [1,2,†], Xiong Xiong Liu [1,2,†], Jiayu Han [3], Ke Hu [4] and Jun Song Chen [1,2,*]

1 School of Materials and Energy, University of Electronic Science and Technology of China, Chengdu 611731, China; jianyangjiang@126.com (J.J.); xiongxiongliu95@126.com (X.X.L.)
2 Center for Applied Chemistry, University of Electronic Science and Technology of China, Chengdu 611731, China
3 Glasgow College, University of Electronic Science and Technology of China, Chengdu 611731, China; 2018190505003@std.uestc.edu.cn
4 Zhuhai Topsun Electronic Technology Co., Ltd., Zhuhai 519060, China; hkfpc@vip.163.com
* Correspondence: jschen@uestc.edu.cn
† These authors contributed equally to this work.

Abstract: Transition metal hydroxides have attracted a lot of attention as the electrode materials for supercapacitors owing to their relatively high theoretical capacity, low cost, and facile preparation methods. However, their low intrinsic conductivity deteriorates their high-rate performance and cycling stability. Here, self-supported sheets-on-wire CuO@Ni(OH)$_2$/Zn(OH)$_2$ (CuO@NiZn) composite nanowire arrays were successfully grown on copper foam. The CuO nanowire backbone provided enhanced structural stability and a highly efficient electron-conducting pathway from the active hydroxide nanosheets to the current collector. The resulting CuO@NiZn as the battery-type electrode for supercapacitor application delivered a high capacity of 306.2 mAh g^{-1} at a current density of 0.8 A g^{-1} and a very stable capacity of 195.1 mAh g^{-1} at 4 A g^{-1} for 10,000 charge–discharge cycles. Furthermore, a quasi-solid-state hybrid supercapacitor (qss HSC) was assembled with active carbon, exhibiting 125.3 mAh g^{-1} at 0.8 A g^{-1} and a capacity of 41.6 mAh g^{-1} at 4 A g^{-1} for 5000 charge–discharge cycles. Furthermore, the qss HSC was able to deliver a high energy density of about 116.0 Wh kg^{-1}. Even at the highest power density of 7.8 kW kg^{-1}, an energy density of 20.5 Wh kg^{-1} could still be obtained. Finally, 14 red light-emitting diodes were lit up by a single qss HSC at different bending states, showing good potential for flexible energy storage applications.

Keywords: self-supported nanoarray; sheets-on-wire; high capacity; flexible quasi-solid-state supercapacitor

check for updates

Citation: Jiang, J.; Liu, X.X.; Han, J.; Hu, K.; Chen, J.S. Self-Supported Sheets-on-Wire CuO@Ni(OH)$_2$/Zn(OH)$_2$ Nanoarrays for High-Performance Flexible Quasi-Solid-State Supercapacitor. *Processes* **2021**, *9*, 680. https://doi.org/10.3390/pr9040680

Academic Editor: David Skoda

Received: 1 March 2021
Accepted: 9 April 2021
Published: 13 April 2021

Publisher's Note: MDPI stays neutral with regard to jurisdictional claims in published maps and institutional affiliations.

Copyright: © 2021 by the authors. Licensee MDPI, Basel, Switzerland. This article is an open access article distributed under the terms and conditions of the Creative Commons Attribution (CC BY) license (https://creativecommons.org/licenses/by/4.0/).

1. Introduction

Environmental problems urge us to develop highly efficient and environment-friendly energy technologies to replace conventional fossil fuels [1–6]. Supercapacitors, as some of the most promising electrochemical energy storage devices, have been extensively studied due to their high power density and long cycle life [7–12]. Based on the different mechanisms of charge storage, the first category could be electrochemical double-layer capacitors (EDLCs). Carbon-based materials with high porosity, large surface area, and relatively high electronic conductivity have usually been considered suitable choices for EDLCs, as they store charges at the surface of the electrodes via electrostatic interaction [13–15]. The second type of supercapacitors stores charges based on faradaic reactions [16–18], and battery-type materials such as Ni(OH)$_2$ are usually used as the electrode materials [11,19]. Because of these electron-transfer processes at the surface or the near-surface region of the electrodes, they usually present a higher charge storage capacity than EDLCs.

For advanced battery-type supercapacitors, the electrode materials should possess high conductivity, abundant active sites, and a relatively low cost. Various materials have been designed and synthesized with enhanced electrochemical performance, such as transition metal-based compounds [20–26]. Among them, transition metal hydroxides have attracted a lot of attention on account of their battery-type feature, high theoretical capacity, facile preparation methods, and low cost. However, their intrinsically low conductivity deteriorates the cycling stability and high-rate performance [21,27–29].

In this work, we reported a self-supported sheets-on-wire composite nanoarray for high-performance battery-type supercapacitor. CuO nanowire array was first fabricated via an electrochemical anodization followed by thermal annealing, which served as support for the hydrothermal growth of $Ni(OH)_2/Zn(OH)_2$ nanosheets, forming a core-shell $CuO@Ni(OH)_2/Zn(OH)_2$ (denoted as CuO@NiZn). The CuO nanowire backbone provided enhanced structural stability and a conducting pathway for highly efficient electron from the hydroxide nanosheets to the current collector. As a result, the as-obtained CuO@NiZn showed a high capacity of 306.2 mAh g^{-1} at a current density of 0.8 A g^{-1}, which is significantly higher than that of CuO (235.8 mAh g^{-1}) and Cu@NiZn (132.4 mAh g^{-1}). After a long charge–discharge test at 4 A g^{-1} for 10,000 cycles, the CuO@NiZn exhibited a retention of 97.3%. Moreover, when a quasi-solid-state hybrid supercapacitor (denoted as qss HSC) was assembled with CuO@NiZn as the positive electrode and activated carbon (AC) as the negative electrode, the device demonstrated a capacity of 125.3 mAh g^{-1} at 0.8 A g^{-1} and a 93.6% retention after 5000 cycles at 4 A g^{-1}. The highest energy density of this qss HSC could reach up to 100.20 Wh kg^{-1}. Even at the highest power density of 16.26 kW kg^{-1}, an energy density of 43 Wh kg^{-1} could still be obtained. Finally, 14 red light-emitting diodes (LEDs) were lit up by a single qss HSC at different bending states, showing good potential for flexible energy storage applications.

2. Results

Figure 1 shows the morphology of different samples prepared after respective treatments. The inset photographs clearly show the distinct transformation of the Cu foam, from light blue to brown and finally to black, indicating the corresponding phase transformations and the formation of new material. It is apparent that the $Cu(OH)_2$ nanowire arrays (denoted as NAs) completely covered the entire surface of the Cu foam (Figure 1a), which showed a uniform 1D nanostructure morphology (Figure 1b). Under a higher magnification (Figure 1c), it is clear that $Cu(OH)_2$ possessed a rodlike structure with a width of about 200 nm. After the thermal conversion, the corresponding CuO maintained the original NA structure (Figure 1d,e) with no apparent collapse. However, a distinct difference could also be observed (Figure 1f) that CuO showed much thinner wirelike subunits with sharp tips. Such a change in the structure could probably be attributed to the decomposition of $Cu(OH)_2$ and the loss of H_2O during the heat treatment. After the hydrothermal growth of Ni/Zn hydroxides, the entire surface of the nanowires was covered with additional materials, giving rise to a much thicker 1D structure (Figure 1g,h). The CuO backbones appeared to be quite robust, which could withstand the hydrothermal condition without loss in structural integrity. The CuO nanowires were covered by small nanosheets with a size of about only 100 nm (Figure 1i), leading to the formation of a sheet-on-wire CuO@NiZn core-shell structure. It should be mentioned that directly using the original $Cu(OH)_2$ NAs for the growth of the hydroxides led to nanosheets growing on the Cu foam (Figure S1) with no presence of the parental 1D NAs. This could be due to the strong destructive effect of the hydrothermal environment, which damaged the $Cu(OH)_2$ NAs. Conversion was thus necessary from the hydroxide to the oxide in order to achieve a high structural stability. Directly growing the metal hydroxides onto the Cu foam substrate would lead to the formation of large nanosheets (Figure S1), which is in accordance with previous reports [30]. Furthermore, the surface structures of the samples were characterized by the Brunner−Emmet−Teller method (Figure S2). It is clear that all the samples showed a type III isotherm, while only CuO@NiZn possessed a type H3

hysteresis loop, suggesting the presence of a porous structure. On the other hand, the other two samples did not exhibit a noticeable hysteresis. This gave rise to a higher surface area of CuO@NiZn of 12.08 m^2 g^{-1} and a larger total pore volume of 0.05 cm^3 g^{-1} than those of CuO (3.34 m^2 g^{-1}, 0.02 cm^3 g^{-1}) and Cu@NiZn (1.33 m^2 g^{-1}, 0.04 cm^3 g^{-1}).

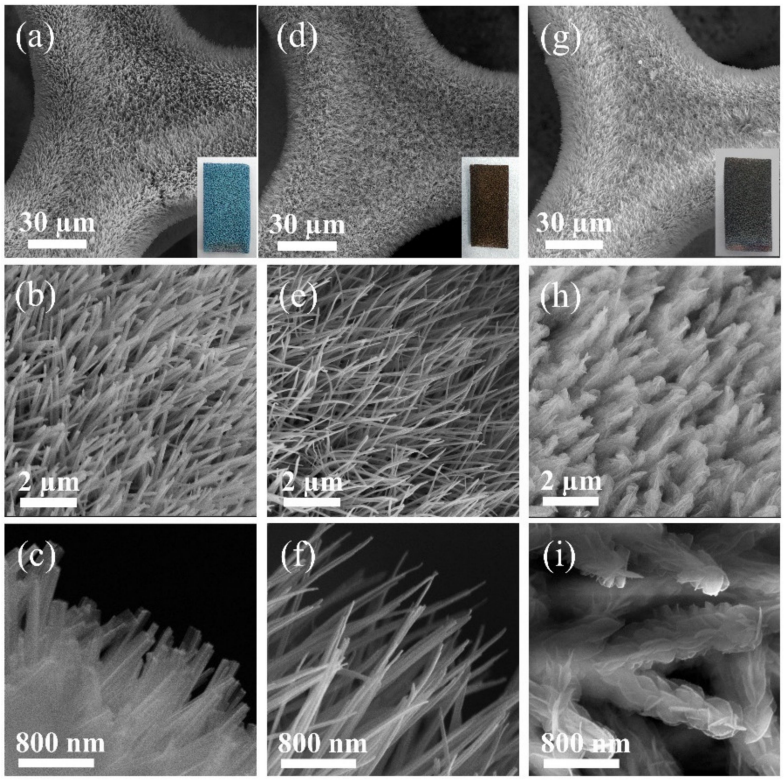


Figure 1. SEM images of the respective treatments. (**a**–**c**) $Cu(OH)_2$, (**d**–**f**) CuO, and (**g**–**i**) CuO@NiZn. The inset in (**a**,**d**,**g**) shows the photographs of $Cu(OH)_2$, CuO, and CuO@NiZn.

Such a sheet-on-wire core-shell structure was verified under transmission electron microscopy (TEM; Figure 2a), where the dense CuO core was wrapped by thin metal hydroxide nanosheets. The visible lattice fringes due to CuO and the hydroxides could be clearly identified at the central and surrounding regions of the composite nanowires, respectively, under high-resolution TEM (HRTEM; insets in Figure 2b,c). The element mapping (Figure 2d) confirmed the uniform distribution of the elements, where Cu was mostly located in the central region of the core-shell structure. Meanwhile, Ni and Zn were distributed in the outer region.

The crystallographic characterization was collected by X-ray diffraction (XRD; Figure 3). It can be observed that in addition to the three very strong peaks due to the Cu foam, there were two minor peaks at about 35° and 39° in CuO. Such weak intensities in these two peaks could be due to the very low heat treatment temperature during the hydroxide-to-oxide conversion, thus giving rise to a relatively poor crystallinity in the resulting CuO. After the hydrothermal treatment, the peaks due to $Ni(OH)_2$ (JCPDS No. 03-0177) and $Zn(OH)_2$ (JCPDS No. 48-1066) could be clearly identified with relatively low intensities [31], and this is quite understandable considering the low hydrothermal temperature employed during synthesis, which may not be able to promote the formation of a highly crystallized structure. At the same time, the peaks due to CuO increased in intensity with one more peak at 46° [32], suggesting that the hydrothermal process helped in the formation of better crystalline CuO. Additionally, directly growing these hydroxides onto the Cu foam gave rise to diffraction peaks with poor intensities (Figure S3), and according to a previous report [33],

the current synthesis has been shown to generate phase-pure Ni-based hydroxide with low crystallinity.

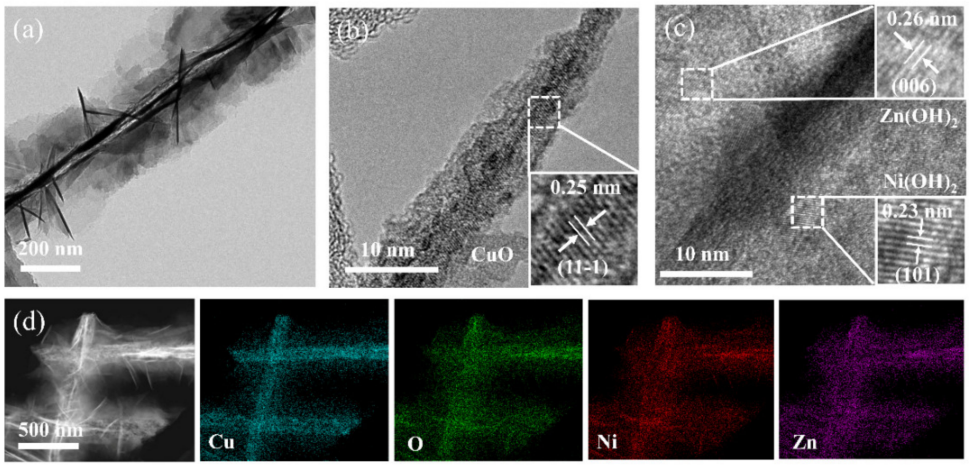


Figure 2. (**a**) TEM, (**b**,**c**) HRTEM, and (**d**) elemental mapping images of CuO@NiZn.

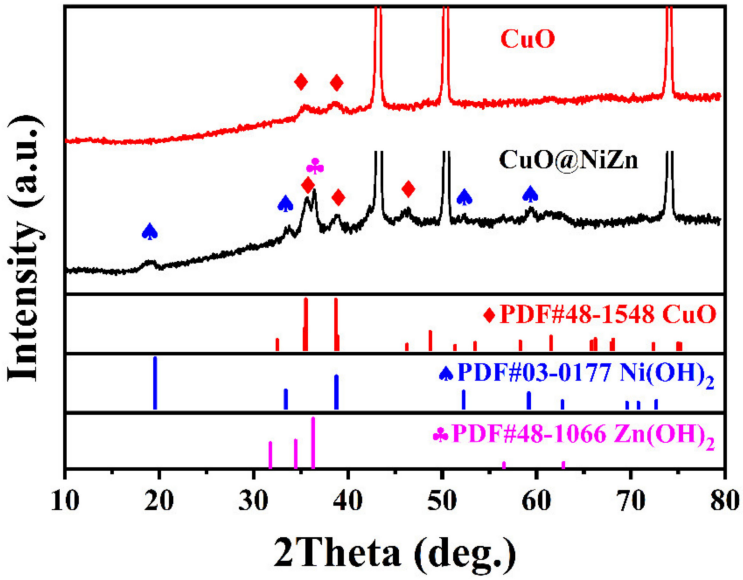


Figure 3. XRD pattern of CuO and CuO@NiZn.

The valence states of different elements of CuO@NiZn were further analyzed by X-ray photoelectron spectroscopy (XPS). The full survey spectrum (Figure S4) confirmed the existence of Cu, O, Ni, and Zn elements. The high-resolution XPS spectrum of Cu 2p (Figure 4a) can be deconvoluted into Cu $2p_{1/2}$ and Cu $2p_{3/2}$ with three satellite peaks located at 962.3, 943.5, and 940.6 eV. These satellite peaks are usually caused by the "shake up" process when excess electrons are excited to higher energy states [34–36]. The Cu $2p_{1/2}$ signal can be fitted into two peaks at 954.4 and 952.2 eV, which can be ascribed to the Cu^{2+} and Cu^0, respectively. The Cu $2p_{3/2}$ signal can also be fitted into two peaks at 934.5 and 932.3 eV, attributing to the Cu^{2+} and Cu^0, respectively. These results are consistent with previous reports [28,29] and can be assigned to CuO (for Cu^{2+}) and the Cu foam substrate (for Cu^0). In the O 1s spectrum (Figure 4b), the peak shows three contributions: the peak at 531.9 eV is typical for adsorbed water (H–O–H), the peak at 531.1 eV for a hydroxyl group (M–OH), and that at 530.3 eV for a metallic oxide (M–O) [37]. Two distinct peaks appear in the Zn 2p spectrum (Figure 4c) at 1044.7 and 1021.6 eV, indicating the existence of Zn^{2+} [38,39]. The high-resolution spectrum of Ni 2p (Figure 4d) shows three satellite

peaks located at 880.1, 865.6, and 862.1 eV [40], following the two main peaks of Ni $2p_{1/2}$ and Ni $2p_{3/2}$ at 856.0 and 873.6 eV, respectively, which can be attributed to the state of Ni^{2+} [28,29,41]. The two peaks at 875.3 and 857.8 eV belong to Ni^{3+}, which might be caused by the partial surface oxidation and has been widely observed in transition metal-based compounds [42,43].

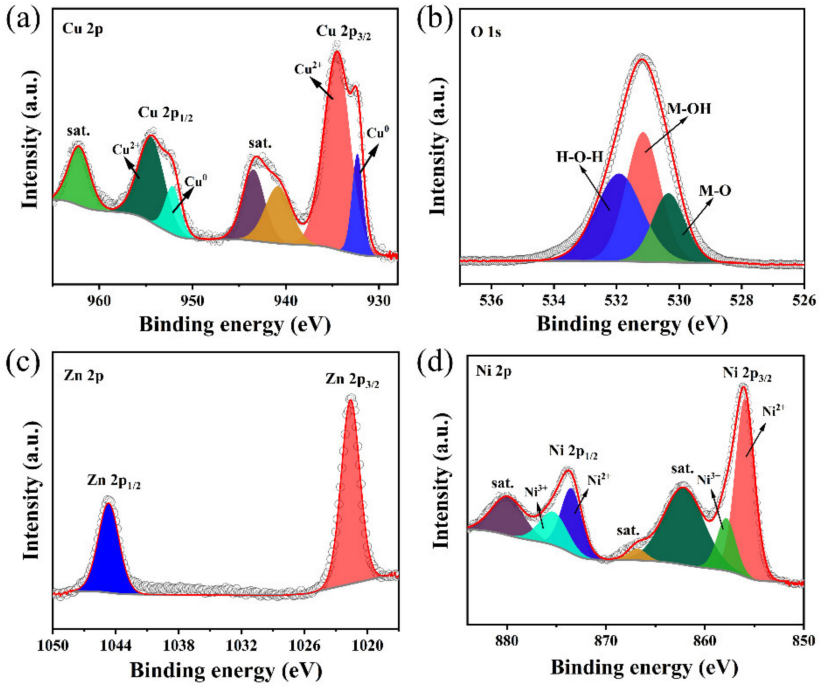


Figure 4. High-resolution XPS spectra of (**a**) Cu 2p, (**b**) O 1s, (**c**) Zn 2p, and (**d**) Ni 2p of CuO@NiZn.

The supercapacitor performance of the as-obtained CuO@NiZn, CuO, and Cu@NiZn were all tested in an alkaline electrolyte, where the potential of the working electrode was relative to that of the reference electrode (saturated calomel electrode, SCE), with a Pt counter electrode. Figure 5a shows the cyclic voltammograms (CVs) of CuO@NiZn at different scan rates from 2 to 50 mV s^{-1}, with oxidation peak at 0.36 V vs. SCE (anodic sweep) and reduction peak at 0.18 V vs. SCE (cathodic sweep) at the scan rate of 2 mV s^{-1}. Such a pair of redox peaks correspond to the following reactions: [41,44,45]:

$$Ni(OH)_2 + OH^- \leftrightarrow NiOOH + H_2O + e^-$$

The contribution of $Zn(OH)_2$ was suggested to accelerate the transport of ions, endowing more efficient faradaic processes [44,46,47]. These redox peaks clearly exhibit the battery-type properties of CuO@NiZn. The capacities (Figure 5b) of 483.1, 400.4, 344.2, 200.5, and 113.8 mAh g^{-1} at the various scan rates can be calculated, which are much higher than the capacity of CuO and Cu@NiZn at the same scan rates (Figure S5), exhibiting the advantages of the current sheet-on-wire composite NAs.

The galvanostatic discharge curves (Figure 5c) of CuO@NiZn were also presented in Figure 5c, showing a typical battery-type behavior with much longer discharge time and plateau than CuO and Cu@NiZn (Figure S4). Thus, the capacity can be calculated to be 306.2, 295.4, 283.8, 281.9, and 281.7 mAh g^{-1} at current densities of 0.8, 2, 4, 10, and 20 A g^{-1}, demonstrating higher capacity than CuO and Cu@NiZn as well (Figure 5d). The long-term cycling performance was tested at 4 A g^{-1} for 10,000 charge–discharge cycles (Figure 5e). Notably, the CuO@NiZn electrode showed a gradual increase in the capacity during the initial few thousand cycles, which could be attributed to a possible activation process [35]. After 10,000 cycles, a remarkable retention of 97.3% could be maintained, demonstrating its excellent reversibility and structural stability. Such a performance is

also considered superior when compared with other reported data (Table S1). In contrast, the capacities of the other two samples declined very rapidly to below 30 mAh g^{-1} for the first 5000 cycles. Electrochemical impedance spectroscopy (EIS) was also carried out with a frequency range of 100 kHz to 0.01 Hz to investigate the change in the interfacial resistance before and after cycling (Figure S6). Interestingly, the semicircle part of the curve in the high-frequency region even decreased in diameter after 10,000 cycles, suggesting a reduced charge transfer resistance. Furthermore, after the long-term performance, the CuO@NiZn electrode still maintained the sheets-on-wire NAs (Figure S7), while the CuO and Cu@NiZn demonstrated severe collapse or rearrangement in the structure, further confirming the superior stability of the as-prepared core-shell NAs.

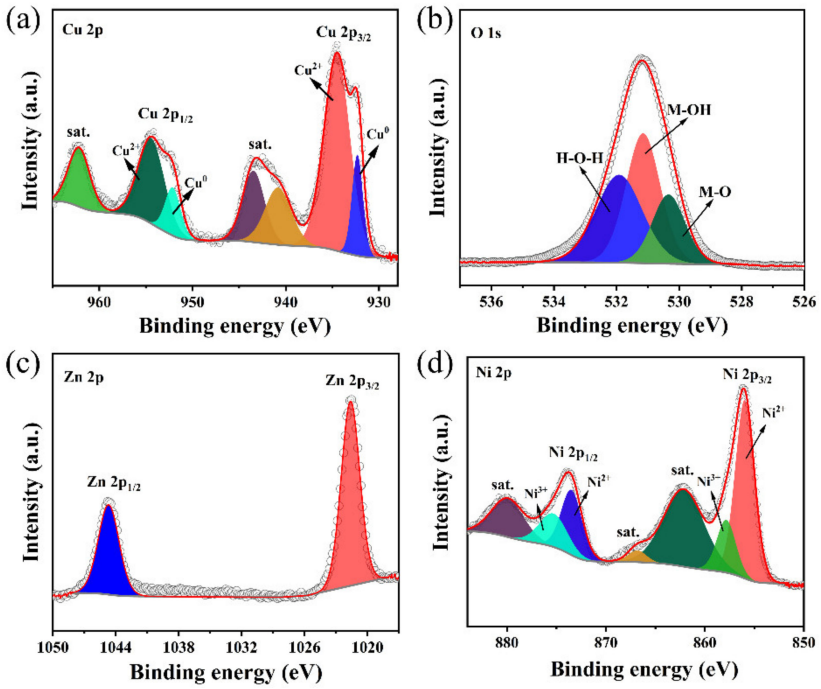


Figure 5. Electrochemical performance. (**a**) Cyclic voltammetry (CV) curves of CuO@NiZn at different scan rates. (**b**) The corresponding capacity calculated from CV curves of three electrodes. (**c**) Galvanostatic charge-discharge (GCD) curves of CuO@NiZn at different current rates. (**d**) The corresponding capacity calculated from GCD curves of three electrodes. (**e**) Long-term charge–discharge performance of three electrodes.

Subsequently, a quasi-solid-state hybrid supercapacitor (qss HSC) was assembled with CuO@NiZn as the positive electrode and active carbon (AC) as the negative electrode to further verify the practical application of the as-prepared electrode. The suitable operating voltage window for the qss HSC was chosen to be 0–1.6 V due to the windows of activated carbon and CuO@NiZn (Figure S8). The CV curves at different scan rates were tested (Figure 6a) with the corresponding specific capacities displayed in Figure 6b. The capacities could be calculated to be 60.5, 59.5, 58.9, 56.0, and 49.5 mAh g^{-1} from 2 to 50 mV s^{-1}. The discharge curves (Figure 6c) implied that the corresponding capacities of 125.3, 116.4, 97.0, 70.6, and 53.7 mAh g^{-1} could be obtained from 0.8 to 20 A g^{-1} (Figure 6d). Figure 6e exhibits the stability at a current rate of 4 A g^{-1}, and the capacity remained to be 43.4 mAh g^{-1} after 5000 cycles. The insets show two photographs with one qss HSC under both flat and bent states powering up 14 red LEDs arranged in the pattern of "SME" (the abbreviation of School of Materials and Energy), indicating good potential for flexible energy storage applications. Furthermore, the maximal energy density of this qss HSC could reach up to 116 Wh kg^{-1}. Even at the highest power density of 7.8 kW kg^{-1}, an energy density of 20.5 Wh kg^{-1} could still be obtained.

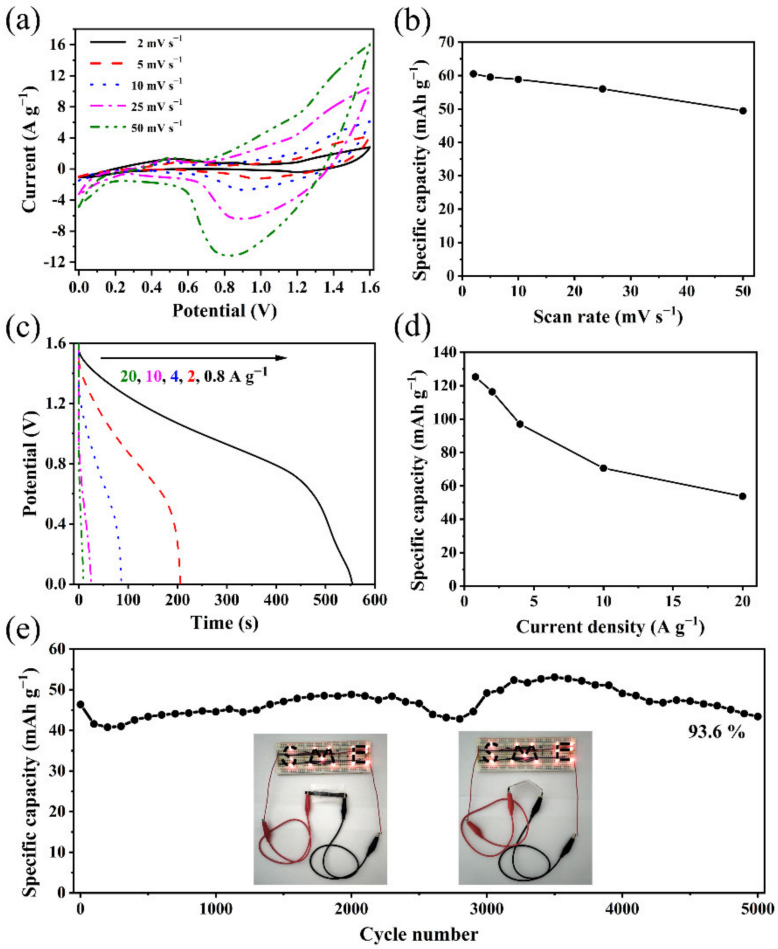


Figure 6. The performance of the quasi-solid-state (qss) CuO@NiZn||activated carbon (AC) hybrid supercapacitor (HSC). (**a**) CV curves of the qss HSC. (**b**) The corresponding capacity calculated from CV curves. (**c**) GCD curves at different current rates. (**d**) The corresponding capacity calculated from GCD curves. (**e**) Long-term charge–discharge performance. The inset in (**e**) shows the photographs of qss HSC powering up 14 red light-emitting diodes (LEDs) arranged in the pattern of "SME" under flat and bend states.

3. Conclusions

In this work, self-supported sheets-on-wire CuO@NiZn nanoarrays were successfully grown on copper foam and applied as battery-type electrode material for a supercapacitor, which delivered a high capacity of 306.2 mAh g^{-1} at a current density of 0.8 A g^{-1}, and a superior rate performance of 281.7 mAh g^{-1} at a high current density of 20 A g^{-1} and a remarkable cycling stability of 97.3% retention after 10,000 cycles. This superior performance could be attributed to its unique structure: the CuO nanowire backbone provided enhanced structural stability and a conducting pathway for a highly efficient electron transport from the hydroxide nanosheets to the current collector. Furthermore, when a quasi-solid-state hybrid supercapacitor was assembled with CuO@NiZn as the positive electrode and activated carbon as the negative electrode, the device demonstrated a capacity of 125.3 mAh g^{-1} at 0.8 A g^{-1}, and a 93.6% retention after 5000 cycles. The maximal energy density of this qss HSC could reach up to 116.0 Wh kg^{-1}. Even at the highest power density of 7.8 kW kg^{-1}, an energy density of 20.5 Wh kg^{-1} could still be obtained. Finally, 14 red LEDs were lit up by a single qss HSC at different bending states, showing good potential for flexible energy storage applications.

Supplementary Materials: The following are available online at https://www.mdpi.com/article/10.3390/pr9040680/s1, Materials and Methods: Figure S1: SEM images of Cu@NiZn and $Cu(OH)_2$@NiZn, Figure S2: N_2 adsorption–desorption isotherm and pore size distribution, Figure S3: XRD pattern of Cu@NiZn, Figure S4: XPS survey spectra of CuO@NiZn, Figure S5: Electrochemical performance in a three-electrode system of CuO and Cu@NiZn, Figure S6: Nyquist plots of CuO@NiZn before and after cycles, Figure S7: SEM images of three electrodes after test, Figure S8: CV curves of AC and CuO@NiZn in a three-electrode system, Table S1: Comparison of the supercapacitor performances.

Author Contributions: Writing—original draft preparation, J.J.; data curation, X.X.L. and J.H.; supervision, K.H.; supervision, writing—original draft preparation, writing—review and editing, J.S.C. All authors have read and agreed to the published version of the manuscript.

Funding: This research was funded by the Fundamental Research Funds for the Central Universities (ZYGX2019J030) and FPC Topsun-UESTC-Research Project (200019).

Institutional Review Board Statement: Not applicable.

Informed Consent Statement: Not applicable.

Data Availability Statement: Not applicable.

Conflicts of Interest: The authors declare no conflict of interest.

References

1. Tarascon, J.M.; Armand, M. Issues and challenges facing rechargeable lithium batteries. *Nature* **2001**, *414*, 359–367. [CrossRef]
2. Aric, A.S.; Bruce, P.; Scrosati, B.; Tarascon, J.M.; Schalkwijk, W.V. Nanostructured materials for advanced energy conversion and storage devices. *Nat. Mater.* **2005**, *4*, 366–377. [CrossRef]
3. Yoo, H.D.; Markevich, E.; Salitra, G.; Sharon, D.; Aurbach, D. On the challenge of developing advanced technologies for electrochemical energy storage and conversion. *Mater. Today* **2014**, *17*, 110–121. [CrossRef]
4. Li, M.; Jun, L.; Zhongwei, C.; Khalil, A. 30 years of lithium-ion batteries. *Adv. Mater.* **2018**, 1800561. [CrossRef]
5. Nitta, N.; Wu, F.; Lee, J.T.; Yushin, G. Li-ion battery materials: Present and future. *Mater. Today* **2015**, *18*, 252–264. [CrossRef]
6. You, J.; Luo, S.; Liu, Y.; Li, G. Interface engineering of highly efficient perovskite solar cells. *Science* **2014**, *345*, 542–546.
7. Simon, P.; Gogotsi, Y.; Dunn, B. Where do batteries end and supercapacitors begin? *Science* **2014**, *343*, 1210–1211. [CrossRef] [PubMed]
8. Simon, P.; Gogotsi, Y. Materials for electrochemical capacitors. *Nat. Mater.* **2008**, *7*, 845–854. [CrossRef] [PubMed]
9. Yu, Z.; Tetard, L.; Lei, Z.; Thomas, J. Supercapacitor electrode materials: Nanostructures from 0 to 3 dimensions. *Energy Environ. Sci.* **2015**, *8*, 702–730. [CrossRef]
10. Miller, J.R.; Burke, A.F. Electrochemical capacitors: Challenges and opportunities for real-world applications. *Electrochem. Soc. Interface* **2008**, *17*, 53–57. [CrossRef]
11. Brousse, T.; Bélanger, D.; Long, J.W. To be or not to be pseudocapacitive? *J. Electrochem. Soc.* **2015**, *162*, 5185–5189. [CrossRef]
12. Arbizzani, C.; Yu, Y.; Li, J.; Xiao, J.; Xia, Y.Y.; Yang, Y.; Santato, C.; Raccichini, R.; Passerini, S. Good practice guide for papers on supercapacitors and related hybrid capacitors for the Journal of Power Sources. *J. Power Sources* **2020**, *450*, 227636. [CrossRef]
13. Zhang, L.L.; Zhao, X.S. Carbon-based materials as supercapacitor electrodes. *Chem. Soc. Rev.* **2009**, *38*, 2520–2531. [CrossRef]
14. Shao, Y.; El-Kady, M.F.; Wang, L.J.; Zhang, Q.; Li, Y.; Wang, H.; Mousavi, M.F.; Kaner, R.B. Graphene-based materials for flexible supercapacitors. *Chem. Soc. Rev.* **2015**, *44*, 3639–3665. [CrossRef]
15. Barbieri, O.; Hahn, M.; Herzog, A.; Kotz, R. Capacitance limits of high surface area activated carbons for double layer capacitors. *Carbon* **2005**, *43*, 1303–1310. [CrossRef]
16. Fleischmann, S.; Mitchell, J.B.; Wang, R.C.; Zhan, C.; Jiang, D.E.; Presser, V.; Augustyn, V. Pseudocapacitance: From fundamental understanding to high power energy storage materials. *Chem. Rev.* **2020**, *120*, 6738–6782. [CrossRef] [PubMed]
17. Lu, Q.; Chen, J.G.G.; Xiao, J.Q. Nanostructured electrodes for high-performance pseudocapacitors. *Angew. Chem. Int. Ed.* **2013**, *52*, 1882–1889. [CrossRef] [PubMed]
18. Lukatskaya, M.R.; Kota, S.; Lin, Z.F.; Zhao, M.Q.; Shpigel, N.; Levi, M.D.; Halim, J.; Taberna, P.L.; Barsoum, M.; Simon, P.; et al. Ultra-high-rate pseudocapacitive energy storage in two-dimensional transition metal carbides. *Nat. Energy* **2017**, *2*, 17105. [CrossRef]
19. Brisse, A.-L.; Stevens, P.; Toussaint, G.; Crosnier, O.; Brousse, T. $Ni(OH)_2$ and NiO based composites: Battery type electrode materials for hybrid supercapacitor devices. *Materials* **2018**, *11*, 1178. [CrossRef] [PubMed]
20. Augustyn, V.; Simon, P.; Dunn, B. Pseudocapacitive oxide materials for high-rate electrochemical energy storage. *Energy Environ. Sci.* **2014**, *7*, 1597–1614. [CrossRef]
21. He, D.; Wang, G.D.; Liu, G.L.; Bai, J.H.; Suo, H.; Zhao, C. Facile route to achieve mesoporous $Cu(OH)_2$ nanorods on copper foam for high-performance supercapacitor electrode. *J. Alloys Compd.* **2017**, *699*, 706–712. [CrossRef]
22. Liu, Y.; Cao, X.Y.; Jiang, D.G.; Jia, D.D.; Liu, J.Q. Hierarchical CuO nanorod arrays in situ generated on three-dimensional copper foam via cyclic voltammetry oxidation for high-performance supercapacitors. *J. Mater. Chem. A* **2018**, *6*, 10474–10483. [CrossRef]

23. Liu, X.X.; He, Q.; Wang, Y.; Wang, J.; Chen, J.S. MOF-reinforced Co_9S_8 self-supported nanowire arrays for highly durable and flexible supercapacitor. *Electrochim. Acta* **2020**, *346*, 136201. [CrossRef]
24. He, Q.; Liu, X.X.; Wu, R.; Chen, J.S. PVP-Assisted Synthesis of Self-Supported Ni_2P@Carbon for High-Performance Supercapacitor. *Research* **2019**, *2019*, 8013285. [CrossRef]
25. Liu, X.X.; Wu, R.; Wang, Y.; Xiao, S.H.; He, Q.; Niu, X.B.; Blackwood, D.J.; Chen, J.S. Self-supported core/shell Co_3O_4@Ni_3S_2 nanowires for high-performance supercapacitors. *Electrochim. Acta* **2019**, *311*, 221–229. [CrossRef]
26. He, Q.; Wang, Y.; Liu, X.X.; Blackwood, D.J.; Chen, J.S. One-pot synthesis of self-supported hierarchical urchin-like Ni_3S_2 with ultrahigh areal pseudocapacitance. *J. Mater. Chem. A* **2018**, *6*, 22115–22122. [CrossRef]
27. Zhang, D.; Shao, Y.; Kong, X.; Jiang, M.; Lei, D.; Lei, X. Facile fabrication of large-area hybrid Ni-Co hydroxide/$Cu(OH)_2$/copper foam composites. *Electrochim. Acta* **2016**, *218*, 294–302. [CrossRef]
28. Zhang, A.T.; Zheng, W.; Yuan, Z.; Tian, J.M.; Yue, L.J.; Zheng, R.K.; Wei, D.; Liu, J.Q. Hierarchical NiMn-layered double hydroxides@CuO core-shell heterostructure in-situ generated on $Cu(OH)_2$ nanorod arrays for high performance supercapacitors. *Chem. Eng. J.* **2020**, *380*, 122486. [CrossRef]
29. Chen, F.; Chen, C.; Hu, Q.; Xiang, B.; Song, T.T.; Zou, X.F.; Li, W.N.; Xiong, B.X.; Deng, M.S. Synthesis of CuO@CoNi LDH on Cu foam for high-performance supercapacitors. *Chem. Eng. J.* **2020**, *401*, 126145. [CrossRef]
30. Tang, Y.; Dong, L.; Wu, H.B.; Yu, X.-Y. Tungstate-modulated Ni/$Ni(OH)_2$ interface for efficient hydrogen evolution reaction in neutral media. *J. Mater. Chem. A* **2021**, *9*, 1456–1462. [CrossRef]
31. Zheng, J.; Zhang, R.; Wang, X.; Yu, P. Hydrothermally synthesized $Ni(OH)_2$@$Zn(OH)_2$ composite with enhanced electrochemical performance for supercapacitors. *Res. Chem. Intermed.* **2018**, *44*, 6637–6648. [CrossRef]
32. Li, Z.; Shao, M.; Zhou, L.; Zhang, R.; Zhang, C.; Han, J.; Wein, M.; Evans, D.G.; Duan, X. A flexible all-solid-state micro-supercapacitor based on hierarchical CuO@layered double hydroxide core–shell nanoarrays. *Nano Energy* **2016**, *20*, 294–304. [CrossRef]
33. Gao, X.R.; Liu, X.M.; Wu, D.J.; Qian, B.; Kou, Z.K.; Pan, Z.H.; Pang, Y.J.; Miao, L.Q.; Wang, J. Significant role of Al in ternary layered double hydroxides for enhancing electrochemical performance of flexible asymmetric supercapacitor. *Adv. Funct. Mater.* **2019**, *29*, 1903879. [CrossRef]
34. Castle, J.E. Use of "Shake-up" Satellites in photoelectron spectra for analysis of oxide layers on metals. *Nat. Phys. Sci.* **1971**, *234*, 93–95. [CrossRef]
35. Chen, J.S.; Gui, Y.; Blackwood, D.J. Self-supported phase-pure Ni_3S_2 sheet-on-rod nanoarrays with enhanced pseudocapacitive properties and high energy density. *J. Power Sources* **2016**, *325*, 575–583. [CrossRef]
36. Chen, J.S.; Guan, C.; Gui, Y.; Blackwood, D.J. Rational design of self-supported Ni_3S_2 nanosheets array for advanced asymmetric supercapacitor with a superior energy density. *ACS Appl. Mater. Interfaces* **2017**, *9*, 496–504. [CrossRef]
37. Yuan, C.Z.; Li, J.Y.; Hou, L.R.; Zhang, X.G.; Shen, L.F.; Lou, X.W. Ultrathin mesoporous $NiCo_2O_4$ nanosheets supported on Ni foam as advanced electrodes for supercapacitors. *Adv. Funct. Mater.* **2012**, *22*, 4592–4597. [CrossRef]
38. Nguyen, T.T.; Balamurugan, J.; Kim, N.H.; Lee, J.H. Hierarchical 3D Zn-Ni-P nanosheet arrays as an advanced electrode for high-performance all-solid-state asymmetric supercapacitors. *J. Mater. Chem. A* **2018**, *6*, 8669–8681. [CrossRef]
39. Bai, J.; Li, X.G.; Liu, G.Z.; Qian, Y.T.; Xiong, S.L. Unusual formation of $ZnCo_2O_4$ 3D hierarchical twin microspheres as a high-rate and ultralong-life lithium-ion battery anode material. *Adv. Funct. Mater.* **2014**, *24*, 3012–3020. [CrossRef]
40. Daiyan, R.; Lu, X.Y.; Tan, X.; Zhu, X.F.; Chen, R.; Smith, S.C.; Amal, R. Antipoisoning nickel-carbon electrocatalyst for practical electrochemical CO_2 reduction to CO. *ACS Appl. Energy Mater.* **2019**, *2*, 8002–8009. [CrossRef]
41. Huang, C.; Hu, Y.; Jiang, S.; Chen, H.C. Amorphous nickel-based hydroxides with different cation substitutions for advanced hybrid supercapacitors. *Electrochim. Acta* **2019**, *325*, 134936. [CrossRef]
42. Park, S.K.; Kim, J.K.; Kang, Y.C. Excellent sodium-ion storage performances of $CoSe_2$ nanoparticles embedded within N-doped porous graphitic carbon nanocube/carbon nanotube composite. *Chem. Eng. J.* **2017**, *328*, 546–555. [CrossRef]
43. Yin, H.; Qu, H.Q.; Liu, Z.T.; Jiang, R.Z.; Li, C.; Zhu, M.Q. Long cycle life and high rate capability of three dimensional $CoSe_2$ grain-attached carbon nanofibers for flexible sodium-ion batteries. *Nano Energy* **2019**, *58*, 715–723. [CrossRef]
44. Liu, Y.; Cao, X.; Cui, L.; Zhong, Y.; Zheng, R.; Wei, D.; Barrow, C.; Razal, J.M.; Yang, W.; Liu, J. Zn-Ni-Co trimetallic carbonate hydroxide nanothorns branched on $Cu(OH)_2$ nanorods array based on Cu foam for high-performance asymmetric supercapacitors. *J. Power Sources* **2019**, *437*, 226897. [CrossRef]
45. Chen, H.C.; Qin, Y.L.; Cao, H.J.; Song, X.X.; Huang, C.H.; Feng, H.B.; Zhao, X.S. Synthesis of amorphous nickel-cobalt-manganese hydroxides for supercapacitor-battery hybrid energy storage system. *Energy Storage Mater.* **2019**, *17*, 194–203. [CrossRef]
46. Gao, J.H.; Xuan, H.C.; Xu, Y.K.; Liang, T.; Han, X.K.; Yang, J.; Han, P.D.; Wang, D.H.; Du, Y.W. Interconnected network of zinc-cobalt layered double hydroxide stick onto rGO/nickel foam for high performance asymmetric supercapacitors. *Electrochim. Acta* **2018**, *286*, 92–102. [CrossRef]
47. Zhang, Q.; Liu, Z.; Zhao, B.; Cheng, Y.; Zhang, L.; Wu, H.-H.; Wang, M.-S.; Dai, S.; Zhang, K.; Ding, D.; et al. Design and understanding of dendritic mixed-metal hydroxide nanosheets@N-doped carbon nanotube array electrode for high-performance asymmetric supercapacitors. *Energy Storage Mater.* **2019**, *16*, 632–645. [CrossRef]